PUBLISHED

This article may be downloaded for personal use only. Any other use requires prior permission of the author and AIP Publishing. This article appeared in *Physics of Fluids, 2018; 30(12):1-15* and may be found at http://dx.doi.org/10.1063/1.5063500

Shen Long, Timothy C. W. Lau, Alfonso Chinnici, Zhao Feng Tian, Bassam B. Dally, and Graham J. Nathan

The influence of aspect ratio on the iso-thermal flow characteristics of multiple confined jets

Physics of Fluids, 2018; 30(12):1-15

© 2018 Author(s).

PERMISSIONS

https://publishing.aip.org/resources/researchers/rights-and-permissions/sharing-content-online/

For institutional or funder-designated repositories (e.g., DOE Pages)

- You may deposit the accepted manuscript immediately after acceptance, using the credit line formatting below
- You may deposit the VOR 12 months after publication, with the credit line and a link to the VOR on AIP Publishing's site

Format for credit lines

- After publication please use: "This article may be downloaded for personal use only. Any other use requires prior permission of the author and AIP Publishing. This article appeared in (citation of published article) and may be found at (URL/link for published article abstract).
- Prior to publication please use: "The following article has been submitted to/accepted by [Name of Journal]. After it is published, it will be found at Link."
- For Creative Commons licensed material, please use: "Copyright (year) Author(s). This article is distributed under a Creative Commons Attribution (CC BY) License."

17 March 2020

http://hdl.handle.net/2440/117943

The influence of aspect ratio on the iso-thermal flow characteristics of multiple confined jets

Shen Long,[a] Timothy C. W. Lau, Alfonso Chinnici, Zhao Feng Tian, Bassam B. Dally, and Graham J. Nathan
Centre for Energy Technology, School of Mechanical Engineering, The University of Adelaide, Adelaide, South Australia 5005, Australia

(Received 28 September 2018; accepted 23 November 2018; published online 20 December 2018)

We report a systematic study of the interaction between four rotationally symmetric jets within a cylindrical chamber obtained with particle image velocimetry, under conditions relevant to a wide range of practical applications including the hybrid solar receiver combustor. The geometry consists of a cylindrical cavity with four inlet jets (representing four burners), which are configured in an annular arrangement and aligned at an inclination angle (α_j) to the axis with a tangential component (azimuthal angle θ_j) to generate a swirl in the chamber. The configurations of $\alpha_j = 25°$ were assessed with two azimuthal angles $\theta_j = 5°$ and 15°, a range of chamber aspect ratios (L_c/D_c), and a fixed nozzle Reynolds number of $Re_D = 10\,500$. The experimental results reveal a significant dependence of the mean and turbulent flow-fields on the aspect ratio L_c/D_c for the values of α_j and θ_j considered here. Three different flow regimes and their controlling parameters were identified within the range $1 \le L_c/D_c \le 3$. The dependence of the flow characteristics on the chamber length L_c was weak within $1.5 < L_c/D_c \le 3$, but significant for $1 \le L_c/D_c \le 1.5$. It was also found that the value of L_c/D_c has a controlling influence on the position and strength of large-scale recirculation regions, together with the extent of flow unsteadiness, although this influence is reduced as θ_j is increased. *Published by AIP Publishing.* https://doi.org/10.1063/1.5063500

I. INTRODUCTION

Multiple confined jets have been widely used in engineering applications such as solar receiver reactors,[1] gas turbine engines,[2] ventilation systems,[3] and multiple-burner combustors.[4] However, comprehensive understanding of the flow-field in these systems is still lacking owing to the large number of controlling parameters, such as jet angles,[5] the extent of confinement by walls,[6] and flow conditions.[7] Of particular interest here are those configurations featuring multiple jets of relevance to the Hybrid Solar Receiver Combustor (HSRC) under development at the University of Adelaide.[8–12] This device features a cavity that is operable as either a solar receiver or a combustion chamber equipped with multiple burners to direct fuel and air into the main cavity and tubular heat exchangers to transfer the thermal energy to the heat transfer fluid. The burners are configured in an annular ring and aligned at an inclination angle (α_j) relative to the axis of the cavity and/or at an azimuthal angle (θ_j) relative to the axis of the burner, resulting in a swirling flow within the main cavity. For conditions in which both $\alpha_j > 0°$ and $\theta_j > 0°$, this arrangement is termed "rotationally symmetric." Previous investigations of the flow-fields within the HSRC revealed a significant effect of the jet angles (α_j and θ_j) on the strength and position of the large-scale recirculation which is critical for achieving desirable flow regimes.[10,11] In addition, the aspect ratio of L_c/D_c has a strong influence on thermal efficiency and capital cost.[9,12] Nevertheless, the dependence of the important flow characteristics on the key geometrical parameters, such as the length (L_c) and diameter (D_c) of the chamber, remains unknown. Hence, the overall objective of the present paper is to provide new understanding of the flow characteristics generated with multiple rotationally symmetric inlet-jets within a cylindrical chamber for a range of chamber aspect ratios L_c/D_c.

Previous studies of flow-fields generated with multiple symmetric jets within a confined space revealed that the flow structure depends strongly on the arrangement and geometrical features of jets.[3,4,10,11,13–16] Chammem *et al.*[3] defined the flow structure downstream from the jet impingement point (P_i) as the "resulting jet flow" and that upstream as the "upstream reverse flow" noting that these flow features are significantly influenced by α_j. The experimental studies of Boushaki and Sautet[4] employing Particle Image Velocimetry (PIV) showed that an increase in α_j from 0° to 30° leads to a significant increase in the magnitude of mean and turbulent velocity fields within the jet merging region. Similarly, the PIV measurements of Long *et al.*[10,11] found a strong dependence on jet angles (α_j and θ_j) of the instantaneous and mean flow-fields generated with multiple symmetric jets. However, to the best of our knowledge, little or no information is available for the key geometrical parameters (e.g., L_c and D_c) of the confined space for multiple jet configurations, although the aspect ratio of geometry has been found to have a significant influence on the flow-fields of free jet impingement[17–19] and cavity flow.[20–22] Importantly, the existing experimental data provide insufficient information to

[a]Author to whom correspondence should be addressed: shen.long@adelaide.edu.au

adequately understand the effect of the aspect ratio on the multiple confined jets in which both α_j and θ_j are variables. Hence, there is a need to obtain reliable, comprehensive, and sufficient data to fully characterize the influence of the chamber aspect ratio L_c/D_c on the mean and RMS (root-mean-square) flow-fields generated with multiple inclined jets in a confined space.

The influence of confinement on the flow-fields has been investigated for a wide range of applications.[16,17,23–27] It has been found that the distance between the jet exit and an end plate, termed "confinement height" (H_c), can significantly influence the position and strength of the recirculation regions, wall jet development, and jet velocity.[17,23,24,26] It has also been found that the influence of the aspect ratio of a confined space is significant for near-field but negligible for far-field within a swirled jet chamber.[27] However, while these previous studies provide useful insight, they are of limited value for model validation due to the lack of information available for the inflow and boundary conditions. Another limit of these studies is that they have been performed almost exclusively for a single jet, which makes it difficult to directly apply to multiple confined jets. In our previous work, Long *et al.*[11] revealed the presence of both an external and internal recirculation zone (ERZ and CRZ) within these configurations. The ERZ and CRZ regions are associated with the entrainment rate (or the recirculation rate) within the chamber, which is important for combustion stabilization and thermal efficiency.[28–30] However, this was assessed for a fixed value of L_c/D_c = 3 so that the influence of L_c/D_c on large-scale recirculation regions is yet to be reported. Hence, additional measurements are needed to identify the influence of the chamber aspect ratio L_c/D_c on the dominant recirculation zones generated by multiple jets within a cylindrical chamber.

To meet the aforementioned needs, the present paper aims to provide new understanding of the iso-thermal flow-fields generated with a Multiple Impinging Jet in a Cylindrical Chamber, termed "MIJCC." More specifically, it aims: (a) to provide a detailed characterization of the flow generated with multiple rotationally symmetric inlet-jets within a cylindrical chamber for the aspect ratios L_c/D_c = 3, 2.5, 2, 1.5, and 1; (b) to identify the influence of the chamber aspect ratio L_c/D_c on both the mean and RMS flow-fields within a cylindrical chamber with multiple jets; and (c) to characterize the dependence of the large-scale recirculation zones (ERZ and CRZ) on the aspect ratio L_c/D_c for low-swirl ($\alpha_j = 25°$ and $\theta_j = 5°$) and high-swirl ($\alpha_j = 25°$ and $\theta_j = 15°$) jet configurations.

II. METHODOLOGY

A. Experimental configurations

The experimental MIJCC configuration is presented schematically in Fig. 1. The design principles have been reported in our previous work,[11] so here only the key geometrical features are discussed. The cavity of the MIJCC consists of a cylindrical chamber with a conical expansion, a secondary concentrator (SC), and four rotationally symmetric inlet jets (N_j = 4). The inlet jets were distributed around the main cavity with a combination of an inclination angle (α_j) and an azimuthal angle (θ_j). The flow leaves the device through an annular outlet around a bluff end-wall.

The values of the key geometrical parameters are listed in Table I. The diameter of the MIJCC was fixed at D_c = 74 mm, while the length of the chamber was set at either L_c = 185 mm, 148 mm, 111 mm, or 74 mm, resulting in aspect ratios of L_c/D_c = 2.5, 2, 1.5, or 1. These ratios were selected to span a sufficient range of flow-features and cover realistic geometrical dimensions for relevant applications. In addition, the chamber length of our previous work L_r = 225 mm (L_r/D_c = 3) was chosen as reference cases for comparison with the present study (labelled with an asterisk in Table II). Two azimuthal angles of θ_j = 5° and 15° were investigated at a fixed inclination angle of α_j = 25°, representing the "low-swirl" and "high-swirl" configurations, respectively. These angles were chosen to generate the two main classes of flow identified in our previous work,[11] which found that either a dominant ERZ or CRZ regime can be generated within the cylindrical chamber, depending on the geometry. All experimental cases are listed in Table II.

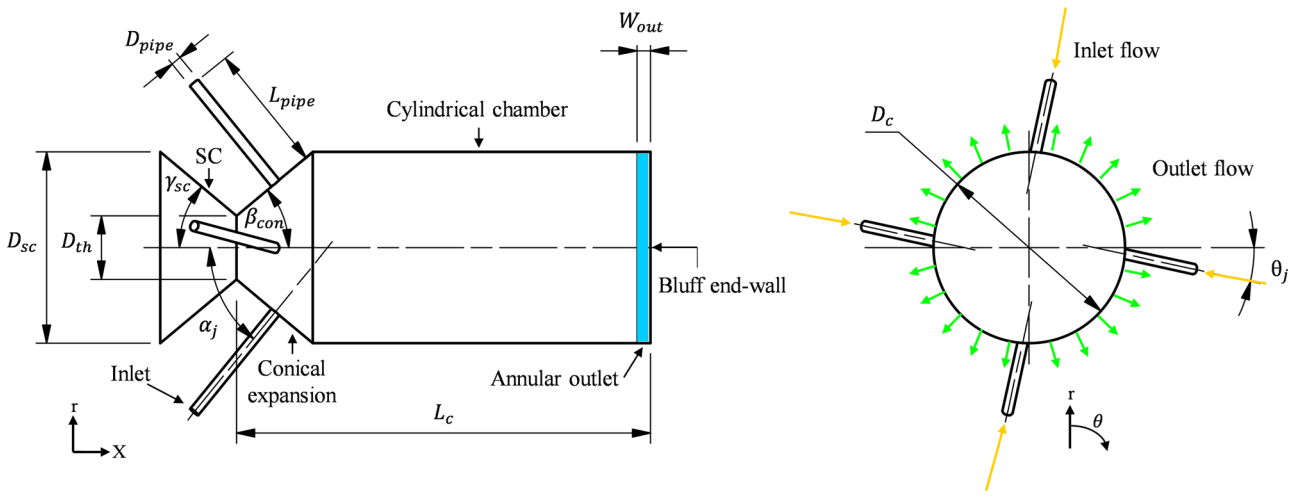

FIG. 1. Schematic diagram of the MIJCC configurations investigated in the present study, showing the key geometrical parameters from the axial cross section (left) and the radial cross section (right).

TABLE I. Values of the geometrical parameters of the MIJCC configurations investigated in the present study.

Dimensions	Description	Value
D_c	Chamber diameter (mm)	74
D_{sc}	Diameter of the SC (mm)	74
D_{th}	Throat diameter (mm)	24.6
D_{pipe}	Inlet pipe diameter (mm)	3.35
L_c	Chamber length (mm)	185, 148, 111, and 74
L_r	Reference chamber length (mm)	225
L_{pipe}	Inlet pipe length (mm)	150
W_{out}	Width of the outlet gap (mm)	3
β_{con}	Conical expansion angle (deg)	40
γ_{sc}	Angle of the SC (deg)	40
α_j	Jet inclination angle (deg)	25
θ_j	Jet azimuthal angle (deg)	5 and 15

TABLE II. The notation for the MIJCC configurations investigated in the present study.

Experiment case no.	Configurations	Jet angles, α_j and θ_j (deg)	Chamber aspect ratio, L_c/D_c
1	MIJCC-05-LD25	25 and 5	2.5
2	MIJCC-05-LD20	25 and 5	2
3	MIJCC-05-LD15	25 and 5	1.5
4	MIJCC-05-LD10	25 and 5	1
5	MIJCC-15-LD25	25 and 15	2.5
6	MIJCC-15-LD20	25 and 15	2
7	MIJCC-15-LD15	25 and 15	1.5
8	MIJCC-15-LD10	25 and 15	1
9*	MIJCC-05-LD30	25 and 5	3
10*	MIJCC-15-LD30	25 and 15	3

B. Experimental arrangement

The present experimental arrangement is similar to that reported previously,[10,11] so only the key experimental apparatus and parameters are described here. Planar Particle Image Velocimetry (PIV) was employed to investigate the mean and RMS flow-fields with the MIJCC configurations. The working fluid was water at ambient temperature, while a closed-loop system was used to recirculate the water from the outlets of the tank to the inlet-pipes. A symmetrical manifold system feeds fluid to four pipes with a length-to-diameter ratio of $L_{pipe}/D_{pipe} \approx 196$ (the straight pipe has a length of $46D_{pipe}$, and the gently curved flexible pipe has a length of $150D_{pipe}$), which ensures that a fully developed pipe flow is achieved at the pipe exit plane.[31] The flow was seeded with hollow glass spheres with a specific gravity of 1.1 and a particle diameter of 12 μm.

The optical arrangement, together with the axial measurement region, is presented schematically in Fig. 2, while the details of the key experimental parameters are listed in Table III. A Nd:YAG laser (Quantel Brilliant B) was used to generate a light sheet with a combination of three cylindrical lenses (Thorlabs). A Charged Coupled Device (CCD) camera (Kodak Megaplus ES2093) was used to capture the PIV images for each measurement.

A total of 1900 PIV image pairs was collected and processed for each experimental condition. An in-house PIV code in MATLAB R2015a (Mathworks) was employed to process the raw images. A multi-grid correlation algorithm with 50% overlap was applied to calculate the displacement of seeding particles and also to minimize noise. Outliers (erroneous vectors) were identified by using an in-house PIV code in the post-processing, which compares the value difference between

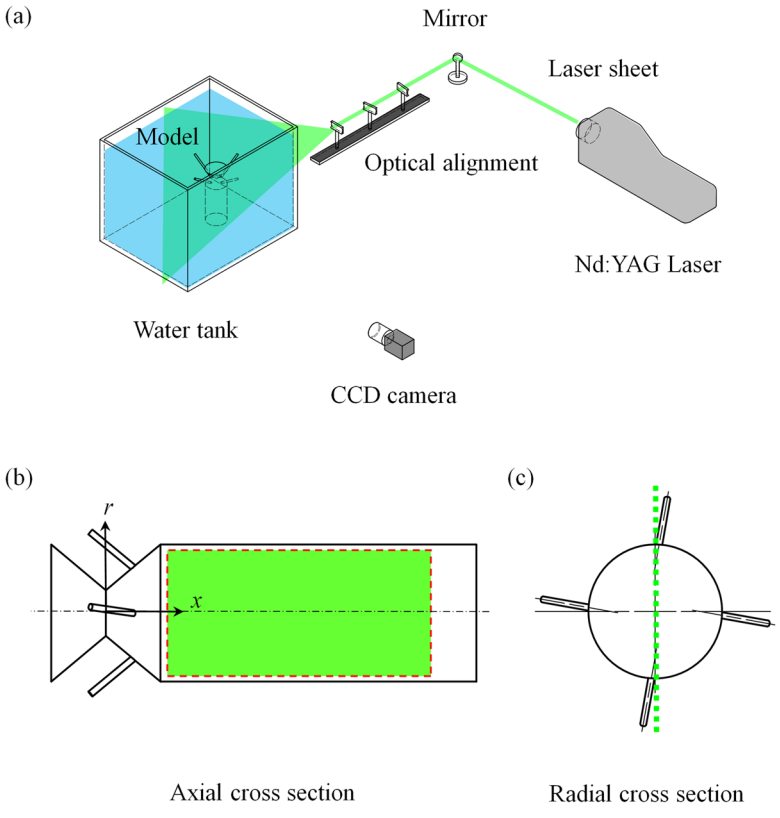

FIG. 2. (a) Schematic diagram of the PIV setup, showing the Nd:YAG laser, optical arrangement, water tank, and camera, (b) the axial measurement region (green box enclosed by a red dashed line) relative to the chamber (not to scale), and (c) the radial cross section, showing the laser sheet.

TABLE III. Details of the key experimental parameters for the present PIV measurements.

Experimental parameters	Value
Bulk mean velocity at the nozzle exit, U_e (m/s)	2.8
Inlet Reynolds number, Re_D	10 500
Laser wavelength (nm)	532
Laser thickness (mm)	1.5
Camera array size (pixels)	1920 × 1080
Measurement region (mm)	123 × 65
Image bit depth (bit)	12
Spatial resolution (mm)	2
Interrogation window (pixels)	32 × 32

the absolute and relative velocities. The average number of outliers was less than approximately 5% of the total vectors, and all outliers were removed from the ensemble.

The overall uncertainty ($\epsilon_{overall}$) associated with the PIV measurements was assessed via a series of systematic analyses, which accounted for the uncertainty derived from the experimental apparatus (2%), calibration (±0.05 mm), laser time-delay (2%), and the image sample size (1%). On these bases, the overall uncertainty for the present PIV measurements was calculated to be $\epsilon_{overall} \approx 5\%$.

III. RESULTS AND DISCUSSION

A. Mean flow fields

Figure 3 presents the contours of the mean axial velocity (U_x) normalized by the nozzle exit velocity (U_e), showing the streamlines, labelled with arrows to indicate the flow direction (white arrows), and magnitude (color map) for the configuration of $\alpha_j = 25°$ and $\theta_j = 5°$ with (a) $L_c/D_c = 2.5$, (b) $L_c/D_c = 2$, (c) $L_c/D_c = 1.5$, and (d) $L_c/D_c = 1$ and for

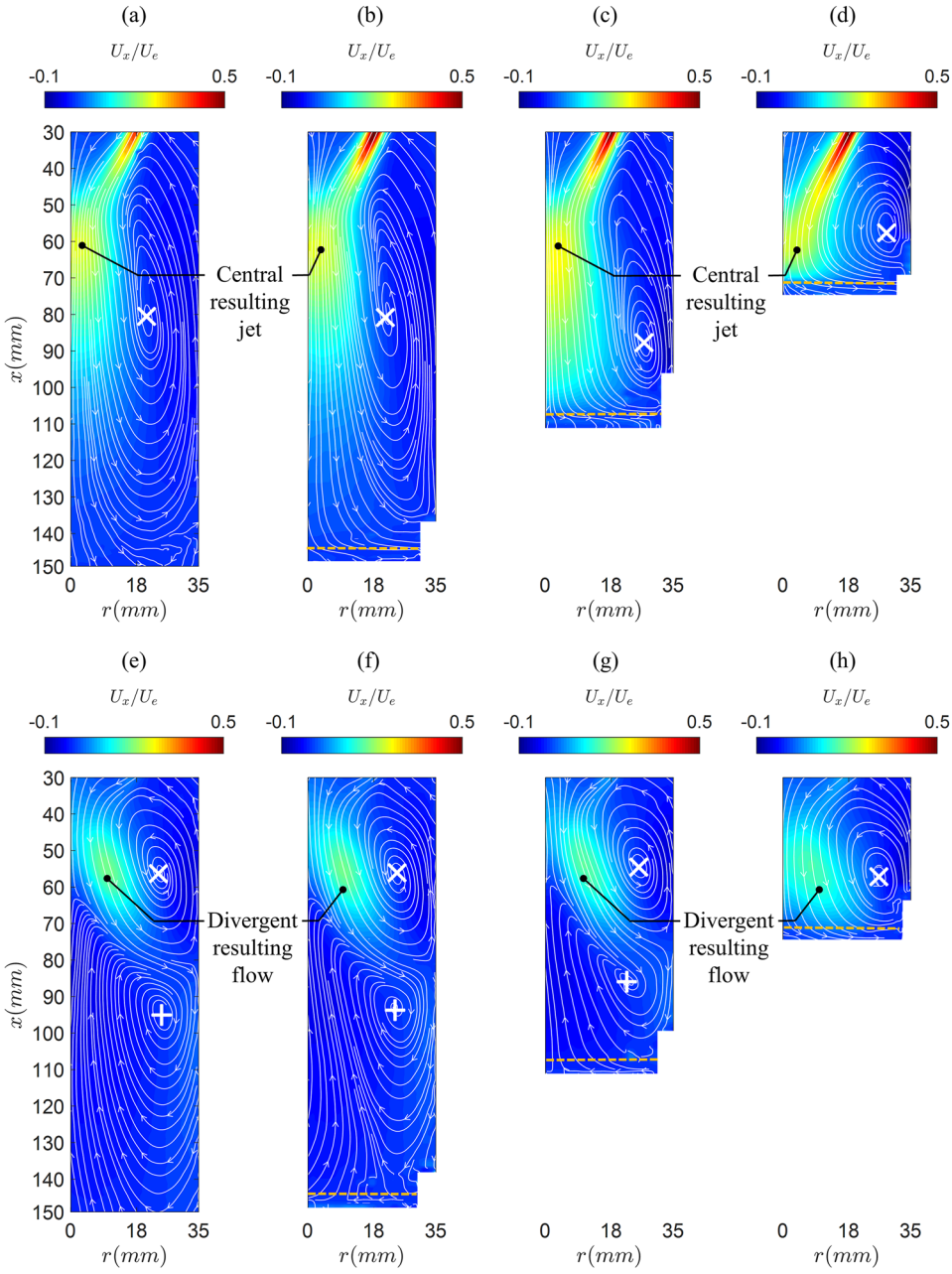

FIG. 3. Mean axial velocity normalized by the nozzle exit velocity (U_x/U_e), showing the streamlines, labelled with arrows to indicate the flow direction (white arrows), and magnitude (color map), for the configuration of $\alpha_j = 25°$ with $\theta_j = 5°$ and 15° for (a) and (e) $L_c/D_c = 2.5$, (b) and (f) $L_c/D_c = 2$, (c) and (g) $L_c/D_c = 1.5$, and (d) and (h) $L_c/D_c = 1$. Here x and r denote the axial and radial locations of the chamber, respectively. The orange dashed line denotes the upstream end of the annular outlet, while the region downstream from this line refers to the exit plane.

the configuration of $\alpha_j = 25°$ and $\theta_j = 15°$ with (e) $L_c/D_c = 2.5$, (f) $L_c/D_c = 2$, (g) $L_c/D_c = 1.5$, and (h) $L_c/D_c = 1$. Here x and r denote the axial and radial locations of the chamber, respectively. The orange dashed line denotes the upstream end of the annular outlet, while the region downstream from this line refers to the exit plane. The location of the vortex-core was determined by a combination of mathematical calculations described by Grosjean *et al.*[32] and visual observation. Owing to the symmetry of the flow in the MIJCC configurations,[11] which was reconfirmed in the preliminary measurements, only half of the measured region is presented here. For the configurations where $\theta_j = 5°$ [Figs. 3(a)–3(d)], it can be seen that a central resulting jet flow occurs for all cases downstream from the merging point (P_{mer}) of the four inlet jets. This resulting flow generates a large vortex (counter-clockwise in Fig. 3, with the vortex-core marked with a white "×") dubbed the external recirculation zone (ERZ). The secondary vortex that was found in the previous work of $L_c/D_c = 3$,[11] if present, must be outside of the imaged region for $L_c/D_c = 2.5$.

It can be seen that the position of the ERZ is almost independent of the chamber length for $L_c/D_c \geq 2$. For example, the axial location of the ERZ vortex-core relative to the throat location, x_{core}, remains constant at $x_{core} \approx 80$ mm as L_c/D_c is reduced from 2.5 to 2 [Figs. 3(a) and 3(b), respectively]. However, as L_c/D_c is further reduced from 2 to 1, x_{core} decreases to ≈60 mm, with the distance between the ERZ vortex-core and the bluff end-wall (Δx_{end}) reduces to $\Delta x_{end} \approx 20$ mm. In addition, this decrease in the aspect ratio also increases the radial location of the ERZ core (r_{core}) from $r_{core} \approx 21$ mm at $L_c/D_c = 2.5$ to $r_{core} \approx 29$ mm at $L_c/D_c = 1$. These findings are attributed to the effect of jet impingement on the bluff end-wall that influences the development of the resulting flow and are consistent with a previous study employing an unconfined single jet.[17] Hence, it can be concluded that the position of the ERZ exhibits a strong dependence on the aspect ratio L_c/D_c for low-swirl configurations ($\theta_j = 5°$), which is most significant for $L_c/D_c < 2$.

Figures 3(a)–3(d) also show that a reduction in the aspect ratio L_c/D_c leads to a significant increase in the velocity magnitude of the inlet-jets upstream from the merging point. For example, the velocity near the merging point increases by ≈35% from $L_c/D_c = 2.5$ [Fig. 3(a)] to $L_c/D_c = 1$ [Fig. 3(d)]. Since the inlet-jet parameters (α_j, θ_j, and U_e) are identical to all cases, the increased value in U_x/U_e is attributed primarily to a reduction in the flow oscillation at and upstream from the merging point as L_c is decreased. This reduction in flow unsteadiness, such as jet flapping or precessing, is addressed later in the paper and has also been widely reported previously for multiple-jet configurations.[16,33,34] For the current MIJCC configurations, a shorter length of the chamber tends to restrict both the "in-plane" and "out-of-plane" motions of the four inlet-jets, which therefore inhibits the flow oscillation that is associated with the interaction between inlet-jets. In addition, the reduction in the chamber length also increases the velocities in the ERZ, reducing the rate of decay in the jets upstream from the merging point.

For the higher-swirl cases with $\theta_j = 15°$ [Figs. 3(e)–3(h)], the ERZ is much shorter and a central recirculation zone (CRZ) also occurs within the measurement region so that no central resulting jet is generated. Instead the flow bifurcates to form a conically divergent resulting flow downstream from the merging point. The cores of the ERZ and CRZ are marked with a white "×" and a white "+," respectively. It can be seen that the axial and radial locations of the vortex-core within the ERZ region remain constant at $x_{core} \approx 56$ mm and $r_{core} = 25$ mm, respectively, regardless of L_c/D_c. By contrast, x_{core} within the CRZ moves upstream from $x_{core} \approx 95$ mm to $x_{core} \approx 86$ mm as L_c/D_c is reduced from 2.5 to 1.5. Importantly, as L_c/D_c is further reduced to 1, the downstream CRZ is no longer observed within the chamber due to insufficient space. The vortex-core of the ERZ at $L_c/D_c = 1$ moves slightly to further downstream ($x_{core} \approx 58$ mm), implying that L_c/D_c influences the ERZ for this case. This also suggests that the dependence of the ERZ on L_c/D_c will be increased if L_c/D_c is further reduced (e.g., $L_c/D < 1$). Hence, for the configurations with large azimuthal angle ($\theta_j = 15°$), the upstream ERZ region is almost independent of the value of L_c/D_c for $L_c/D_c \geq 1.5$ but becomes significant for $L_c/D_c < 1.5$, while the downstream CRZ region depends strongly on all values of L_c/D_c considered here.

Figure 4 presents the evolution of normalized mean axial velocity along the axis (U_c/U_e) for all MIJCC configurations investigated here. The PIV data from our previous work[11] of $L_c/D_c = 3$ are also included. Each mean velocity measurement has been performed from the time-average of the 1900 PIV image pairs. In each figure, the dashed line denotes the value of $U_c/U_e = 0$, while the dotted lines color-matched with data points refer to the locations of the bluff end-wall. The jet merging point, P_{mer}, refers to the location of the maximum velocity along the centerline of the chamber [$(U_c/U_e)_{max}$], the stagnation point, P_s, as the most upstream axial location of the velocity zero-crossing ($U_c/U_e = 0$), which also denotes the most downstream location of the resulting flow, and the point of the minimum axial velocity, P_{min}, as the axial location of the minimum velocity [$(U_c/U_e)_{min}$].

For the configurations of $\theta_j = 5°$ [Fig. 4(a)], it can be seen that a decrease in the aspect ratio L_c/D_c does not change the magnitude or location of U_c/U_e at the merging point, with $(U_c/U_e)_{max} \approx 0.26$ at $x/L_c = 0.27$ for all cases. However, downstream from the merging point, the evolution of U_c/U_e is strongly influenced by L_c/D_c. For example, as L_c/D_c reduces from 2.5 to 1.5, the location of the stagnation point moves upstream from $x/L_c = 0.65$ to 0.5, while the decay of U_c/U_e decreases significantly for $L_c/D_c = 1.5$. This is possibly caused by the effect of the end-wall on the development of central resulting jet flow that reduces the entrainment rate between the jet and surrounding fluids.[17,35] Importantly, large data fluctuations were found at $x/L_c \approx 0.48$, with RMS ≈ 0.037 for the case of $L_c/D_c = 1.5$, which is consistent with the strong gradients caused by the combined effects of a radial outlet flow, a bluff end-wall, and a cylindrical chamber. In addition, for $L_c/D_c = 1$ where the bluff end-wall closely approaches the location of the merging point, the central resulting flow is almost absent [see also Fig. 3(d)] due to the confinement effect from the cylindrical walls, while the decay of U_c/U_e is the highest for all cases. Hence, it can be concluded that, for the case of $\theta_j = 5°$, reducing the aspect ratio L_c/D_c significantly inhibits the axial development of the central resulting flow for $L_c/D_c < 2$.

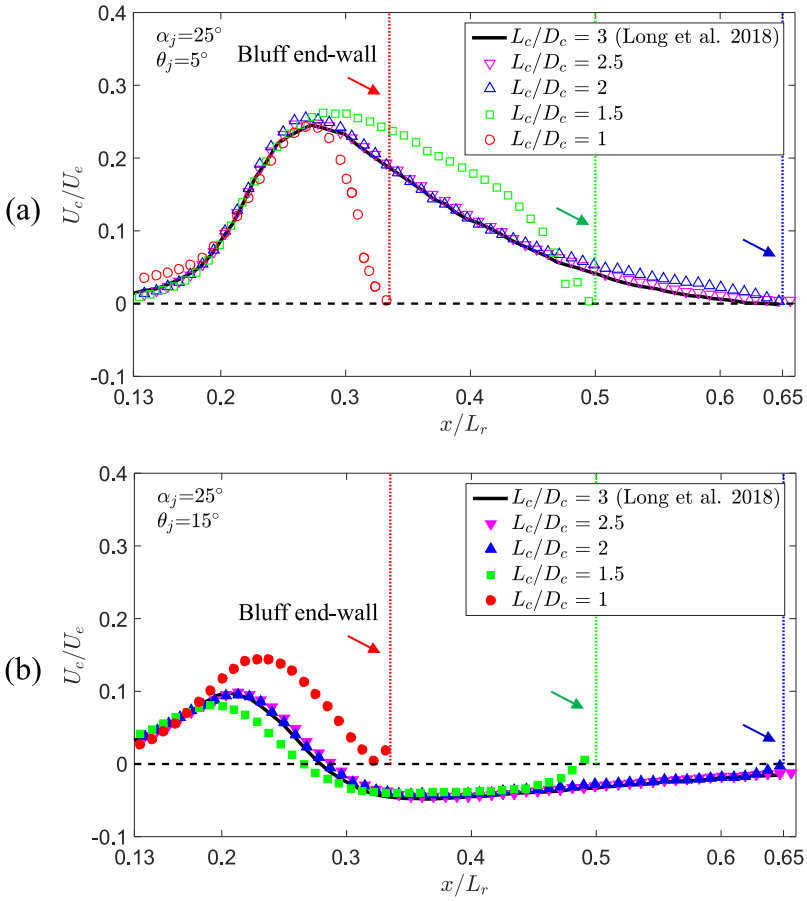

FIG. 4. Evolution of normalized mean axial velocity along the centerline of the MIJCC configurations (U_c/U_e), as a function of the reference chamber length (L_r) for the cases of (a) α_j = 25° and θ_j = 5°, (b) α_j = 25° and θ_j = 15°, and for aspect ratios of L_c/D_c = 1–3. The dotted lines color-matched with data points refer to the locations of the bluff end-wall. For clarity, only one in two data points is presented.

For the θ_j = 15° case [Fig. 4(b)], it can be seen that the evolution of U_c/U_e along the axis is almost independent from L_c/D_c for $L_c/D_c \geq 2$. The value of $(U_c/U_e)_{max}$ is approximately 0.1 at $x/L_c = 0.21$, while $(U_c/U_e)_{min}$ is approximately −0.05 at $x/L_c = 0.37$ for the cases of L_c/D_c = 2–3. This shows that the locations of both the merging and stagnation points are independent from L_c/D_c for these cases. However, as the value of L_c/D_c reduces to 1.5, the location of the merging point moves slightly upstream (from x/L_c = 0.22 to 0.19), while magnitude of $(U_c/U_e)_{max}$ reduces by 15%. The axial extent of the negative velocity flow ($U_c/U_e < 0$) was also found to be reduced due to a shorter L_c, although both the magnitude and location of $(U_c/U_e)_{min}$ remain the same. For the shortest L_c considered here (L_c/D_c = 1), no negative velocity region is present owing to the absence of the CRZ [see also Fig. 3(h)]. In addition, the location of the merging point progresses further downstream to $x/L_c = 0.24$, while the value of $(U_c/U_e)_{max}$ increases to 0.15 for L_c/D_c = 1. This indicates an increase in the size and intensity of the ERZ for L_c/D_c = 1, which also highlights the effect of the bluff end-wall on the development of divergent resulting flow. Hence, for the θ_j = 15° case, the aspect ratio of L_c/D_c can influence the flow characteristics within the CRZ for $L_c/D_c > 1$ or within the ERZ for $L_c/D_c < 2$.

Overall, the evolution of $U_c/U_e \geq 0$ is almost independent from the value of the chamber length L_c before the resulting flow approaches the bluff end-wall of the chamber, while this dependence increases significantly as L_c is further reduced. This is also consistent with the qualitative flow patterns in Fig. 3 as both the recirculation regions and resulting flow are changed for certain values of L_c depending on the configurations. Taken together, it can be concluded that the mean velocity field exhibits a strong dependence on the axial location of the resulting flow.

Figure 5 presents the evolution of the inverse mean axial velocity of the central resulting jet flow (U_e/U_c) as calculated on the equivalent axial coordinate from the jet origin

$$x^* = x_0 + (x - x_{mer}), \tag{1}$$

where x_{mer} denotes the distance between the throat and merging point and x_0 denotes the distance along the local axis of each jet between the pipe exit and merging point (see also the inset of Fig. 5). The cases with θ_j = 15° are not reported due to the absence of a resulting jet flow along the centerline of the chamber. However, the data for L_c/D_c = 3 and θ_j = 0° reported previously[10] for non-swirled jets are included as a reference, and also included are the free pipe jet data of Xu and Antonia[36] representing the unconfined single jet case. The axial coordinate is normalized by the equivalent jet exit diameter,

$$D_e = \sqrt{N_j} D_{pipe}, \tag{2}$$

where N_j denotes the number of jets and D_e is the diameter of an equivalent circular pipe with the same exit area as the four inlet pipes. Here the merging and stagnation points (P_{mer} and P_s) denote the most upstream and downstream of the resulting flow, respectively. It can be seen that, for all cases with a non-zero azimuthal angle ($\theta_j > 0°$), the decay of U_e/U_c along the

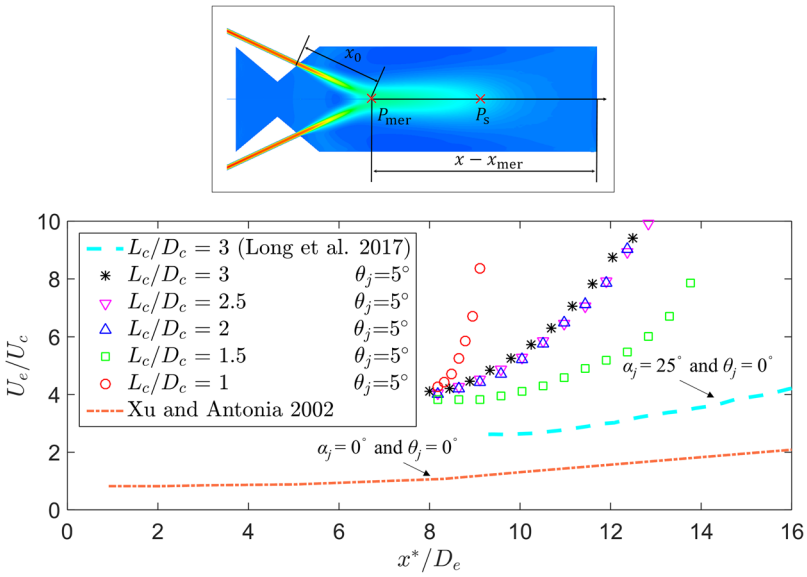

FIG. 5. Evolution of the inverse mean axial velocity of the central resulting jet flow (U_e/U_c) along the axis of the MIJCC for the case of $\alpha_j = 25°$ and $\theta_j = 5°$ for aspect ratios of L_c/D_c = 1–3. The equivalent axial coordinate, x^*, and the equivalent jet exit diameter, D_e, are expressed in Eqs. (1) and (2), respectively.

centerline of the chamber is significantly greater than the non-swirled jet ($\theta_j = 0°$) or single jet ($N_j = 1$) configurations within $8 \le x^*/D_e \le 16$, regardless of the value of L_c/D_c. This is due to the presence of θ_j that increases the "out-of-plane" motion from the inlet jets, which implies that the additional azimuthal angle of the multiple-jet configurations substantially increases the centerline velocity decay of the resulting flows.

Figure 5 also shows that, for the configurations with $\theta_j = 5°$, a decrease in L_c/D_c from 3 to 2 leads to a decrease of only 5% in the rate of decay, i.e., $\Delta(U_e/U_c)/\Delta(x^*/D_e)$, while a decrease in L_c/D_c from 2 to 1.5 leads to a decrease in the rate of decay by up to 40% at $x^*/D_e = 13$. The rate of centerline decay has long been used as a measure of rate at which the jet flow exchanges momentum with the surrounding flow.[37] Hence this step-change reduction at shorter chambers indicates a step change in the intensity of the ERZ. However, for the shortest chamber length considered here ($L_c/D_c = 1$), the rate of decay is the highest [$\Delta(U_e/U_c)/\Delta(x^*/D_e) \approx 4$], with $U_e/U_c \approx 8.5$ at $x^*/D_e \approx 9$. This is due to the insufficient space downstream from the merging point, which causes the distance between the merging and stagnation points to approach zero [$(x_{Ps} - x_{Pmer}) \approx 0$], implying that the resulting flow is almost absent. Hence, it can be concluded that the rate of decay of central resulting flow depends strongly on the distance between the merging and stagnation points—for the low-swirl configurations ($\alpha_j = 25°$ and $\theta_j = 5°$) considered here.

B. Turbulent flow fields

Figure 6 presents the evolution of the axial RMS (u') and radial RMS (v') velocities, normalized by the nozzle exit velocity (U_e), along the centerline of the MIJCC for all experimental cases. Note that the legends are identical to all cases with the same θ_j for all figures in the paper. For the $\theta_j = 5°$ cases [Figs. 6(a) and 6(b)], it can be seen that a decrease in L_c/D_c leads to a substantial decrease (≈20%) in both u'/U_e and v'/U_e, particularly where $L_c/D_c \le 1.5$. This suggests that the flow unsteadiness is substantially reduced as the chamber length is decreased. However, for the $\theta_j = 15°$ cases [Figs. 6(c) and 6(d)], both the magnitudes of u'/U_e and v'/U_e are almost independent from L_c for all aspect ratios investigated here, while the difference in the magnitude of u'/U_e and v'/U_e is typically within 10%. This weaker dependence of the centerline velocity fluctuations on L_c/D_c for $\theta_j = 15°$ than for $\theta_j = 5°$ provides further evidence of the reduced influence of the chamber aspect ratio on flow unsteadiness (e.g., precession) for higher azimuthal angles.

It is also worth noting that for both $\theta_j = 5°$ and $\theta_j = 15°$ configurations, a significant reduction in u'/Ue and an increase in v'/Ue were measured in the region where the resulting flow approaches the bluff end-wall (≈5% of the total length of L_c before the end-wall). This is most significant for the cases where $L_c/D_c \le 1.5$. That is, the impingement of the resulting flow on the bluff end-wall acts both to amplify the velocity fluctuations in the radial direction (v') and to inhibit the axial velocity fluctuations (u') within the impingement region.

The results in Figs. 4–6 show that both the mean and RMS flow-fields are typically independent from the value of $L_c/D_c = 3$. Hence, subsequent analyses are performed only for the range of $1 \le L_c/D_c \le 2.5$.

Figure 7 presents the radial profiles of the mean axial (U_x), axial RMS (u'), and radial RMS (v') velocities, normalized by the nozzle exit velocity (U_e), at the jet merging point for all experimental conditions. (The $L_c/D_c = 3$ case was not included here because the measurements are almost identical to the $L_c/D_c = 2.5$ case.) The results in Fig. 7(a) show that, for the $\theta_j = 5°$ cases, the value of U_x/U_e at the merging point is almost independent from the chamber length for $1 < L_c/D_c \le 2.5$. The peak mean velocity $(U_c/U_e)_{max}$ occurs on or near to the central axis, while the region of negative velocity is typically limited to $r/D_c \ge 0.3$ for all cases. This indicates that the radial extent of the ERZ does not change significantly with the value of L_c/D_c for $L_c/D_c > 1$. However, as L_c/D_c is decreased to 1, the magnitude of velocity within $r/D_c \ge 0.2$ increases by approximately 10% and the radial location of negative velocity extends to $r/D_c \ge 0.4$. This highlights the influence of the bluff end-wall on the flow field at and around the merging point for all cases.

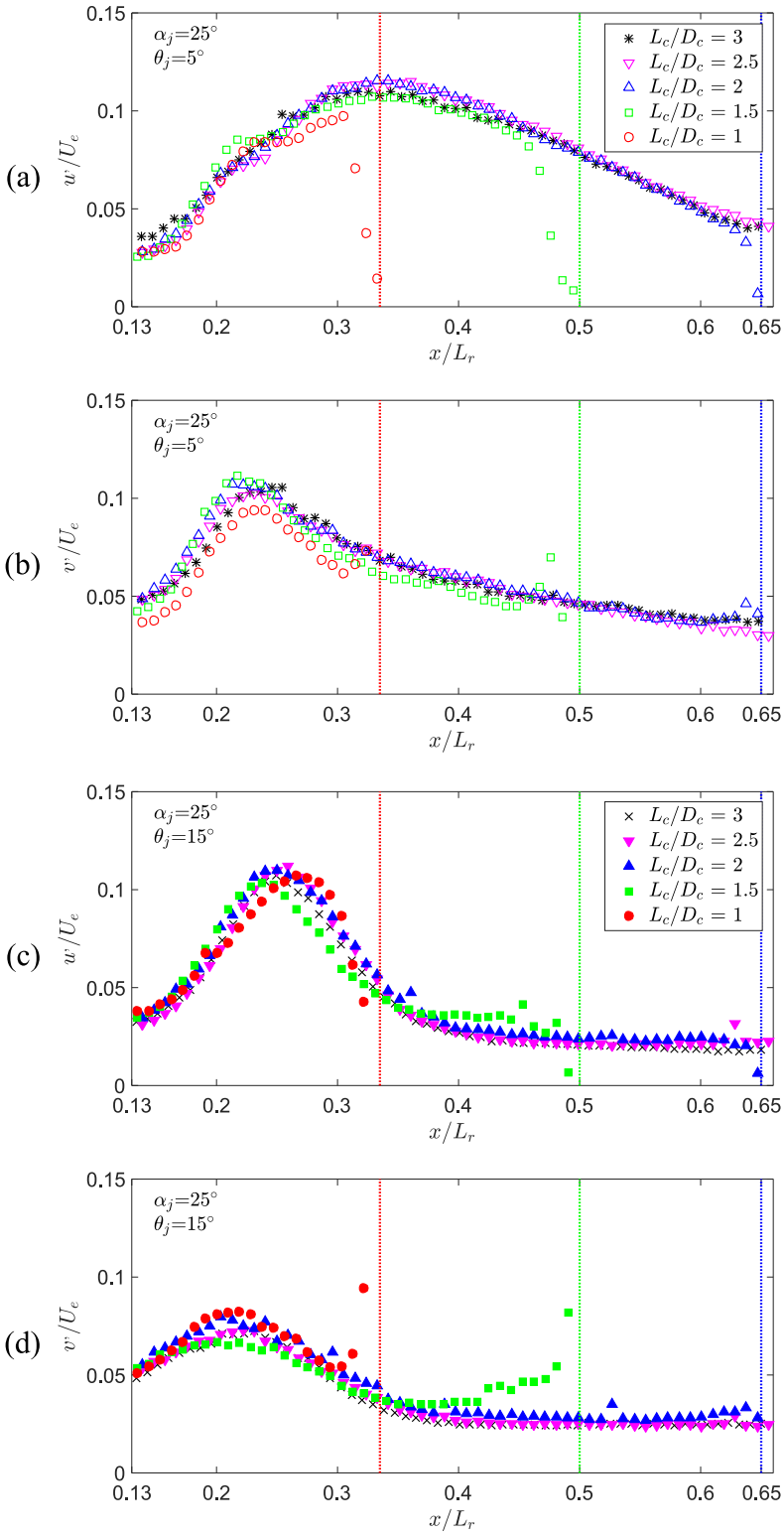

FIG. 6. Evolution of the axial RMS (u') and radial RMS (v') velocities, normalized by the nozzle exit velocity (U_e), along the centerline of the MIJCC for the cases of (a) and (b) $\alpha_j = 25°$ and $\theta_j = 5°$, (c) and (d) $\alpha_j = 25°$ and $\theta_j = 15°$, and for aspect ratios of L_c/D_c = 1–3. For clarity, only one in two data points is presented and the legends are identical to all cases with the same θ_j.

The results in Figs. 7(b) and 7(c) also show that a decrease in L_c/D_c leads to a maximum reduction of 20% in the value of u'/Ue, while the value of v'/Ue remains almost independent from the L_c/D_c. The location of $(u'/Ue)_{max}$, which corresponds well with the maximum value of the mean velocity gradient presented in Fig. 7(a), moves from $r/D_c \approx 0.16$ to $r/D_c \approx 0.09$ and its magnitude decreases from $(u'/Ue)_{max} \approx 0.12$ to ≈ 0.09 as L_c/D_c is decreased from 2.5 to 1. However, the value of $(v'/Ue)_{max}$ is approximately 0.08 at the central axis ($r/D_c = 0$) for all cases. This indicates that a decrease in L_c/D_c from 2.5 to 1 tends to inhibit the axial velocity fluctuation but not to influence significantly the radial velocity fluctuation at the merging point. As a large fluctuation of velocity is commonly associated with flow unsteadiness,[33] this provides further evidence that decreasing the aspect ratio tends to reduce the flow unsteadiness within the jet-interaction region for low-swirl configurations ($\alpha_j = 25°$ and $\theta_j = 5°$).

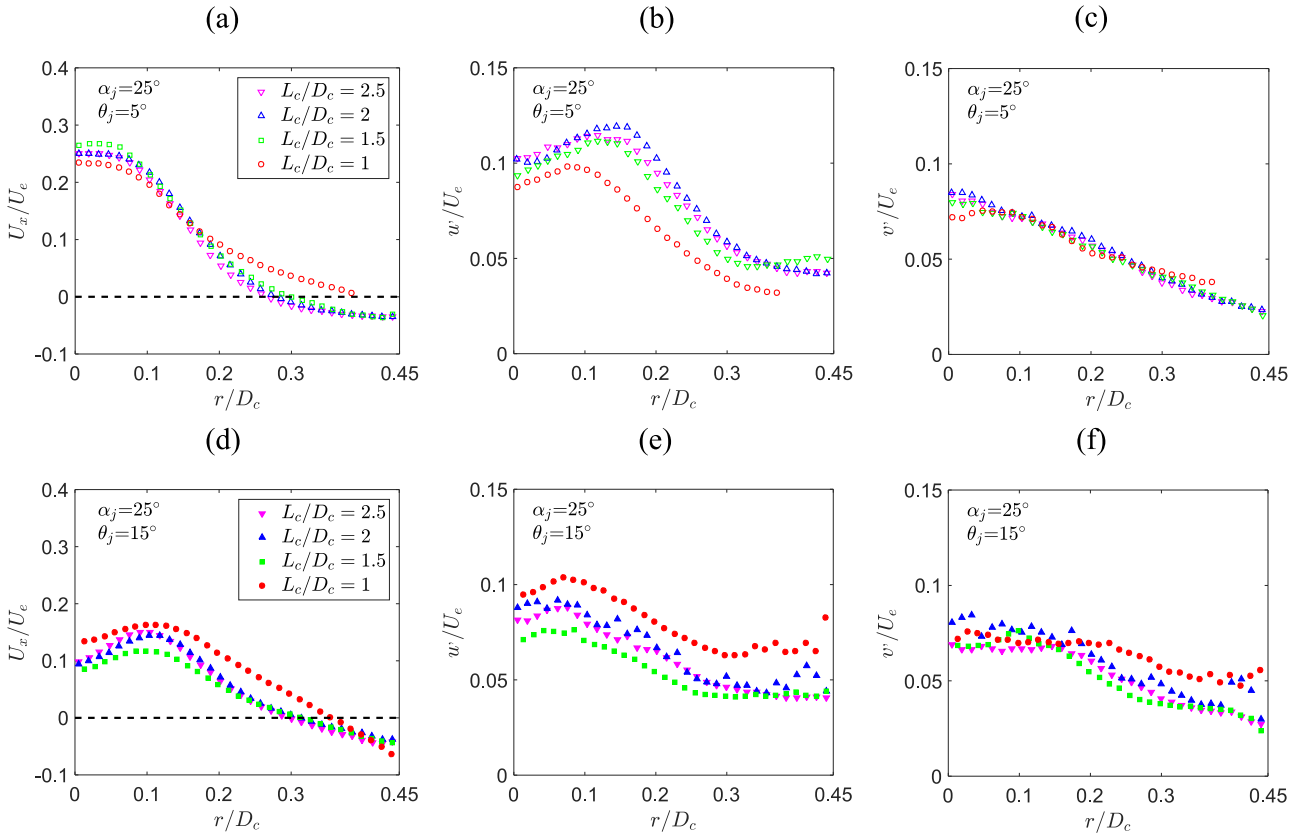

FIG. 7. Radial profiles of the mean axial (U_x), axial RMS (u'), and radial RMS (v') velocities, normalized by the nozzle exit velocity (U_e), at the jet merging point for the cases of (a)–(c) $\alpha_j = 25°$ and $\theta_j = 5°$, (d)–(f) $\alpha_j = 25°$ and $\theta_j = 15°$, and for aspect ratios of $L_c/D_c = 2.5$, 2, 1.5, and 1. Here D_c denotes the diameter of the MIJCC and the legends are identical to all cases with the same θ_j.

For the $\theta_j = 15°$ configurations, the velocity peak $(U_c/U_e)_{max}$ occurs at $r/D_c \approx 0.1$ for all cases [Fig. 7(d)]. It can also be seen that the mean axial velocity decreases slightly as L_c/D_c is decreased from 2.5 to 1.5, with a maximum 20% reduction in U_x/U_e at $r/D_c \approx 0.1$. However, the value of U_x/U_e increases significantly as L_c/D_c is further reduced to 1, and the maximum increase is around 70% within $r/D_c \geq 0.2$. The trend of an increased U_x/U_e for the case where L_c/D_c approaches 1 is possibly caused by the increased strength of the divergent resulting flow for $\theta_j = 15°$ cases, as shown qualitatively in Fig. 3.

The radial profiles of RMS velocities in Figs. 7(e) and 7(f) show that the effect of L_c/D_c on the velocity fluctuations is non-linear since both the values of u'/Ue and v'/Ue decrease as L_c/D_c is decreased from 2.5 to 1.5 and then increase as L_c/D_c is further decreased to 1. Interestingly, the CRZ is detected for $L_c/D_c \geq 1.5$, but not for $L_c/D_c = 1$ (see also Fig. 3). This suggests that the presence of a CRZ damps velocity fluctuations in the high-swirl configurations ($\theta_j = 15°$). Nevertheless, the case $L_c/D_c = 1$ has a different trend to the other cases in the mean and RMS velocity fields due to the absence of the central resulting jet flow for $\theta_j = 5°$ configurations or the CRZ region for $\theta_j = 15°$ configurations.

Overall, it can be concluded that a decrease in the aspect ratio L_c/D_c leads to a decrease in velocity fluctuations for most cases, although the effects are non-linear. That is, increasing L_c/D_c in this range tends to increase interaction with the wall, and hence the amplification of large-scale eddies in the flow.

Figure 8 presents the radial profiles of the ratio of axial and radial RMS velocities (u'/v') and the Reynolds shear stresses ($\langle uv \rangle / U^2{}_c$) at the merging point for all experimental conditions. For the configurations of $\theta_j = 5°$ [Fig. 8(a)], it can be seen that the value of u'/v' exhibits two peaks, one in the shear layer ($r/D_c \approx 0.15$), consistent with an unconfined single jet,[38] and the other in the near wall region ($r/D_c \approx 0.45$). These locally high values imply a high degree of anisotropy in these regions, consistent with an important role of large-scale turbulence. In addition, a decrease in L_c/D_c tends to reduce the value of u'/v' along the cylinder radius (r), with the most significant reduction occurring for $L_c/D_c = 1$. By contrast, for the configurations where $\theta_j = 15°$ [Fig. 8(b)], the value of u'/v' typically varies between 1.5 and 1 for all cases, so that the effect of L_c/D_c on u'/v' is relatively small. This indicates that, first, the variation of anisotropy at the merging point is more significant for $\theta_j = 5°$ than that for $\theta_j = 15°$, regardless of the value of L_c/D_c, and second, the influence of L_c/D_c on the anisotropy is more significant for the ERZ dominated regime ($\theta_j = 5°$) than that for the CRZ dominated regime ($\theta_j = 15°$).

Figures 8(c) and 8(d) also show that a decrease in L_c/D_c leads to a decrease in the Reynolds stresses at the merging point for both the $\theta_j = 5°$ and $\theta_j = 15°$ configurations, although it is most significant for $\theta_j = 5°$. This provides further evidence that reducing L_c/D_c reduces large-scale interactions between

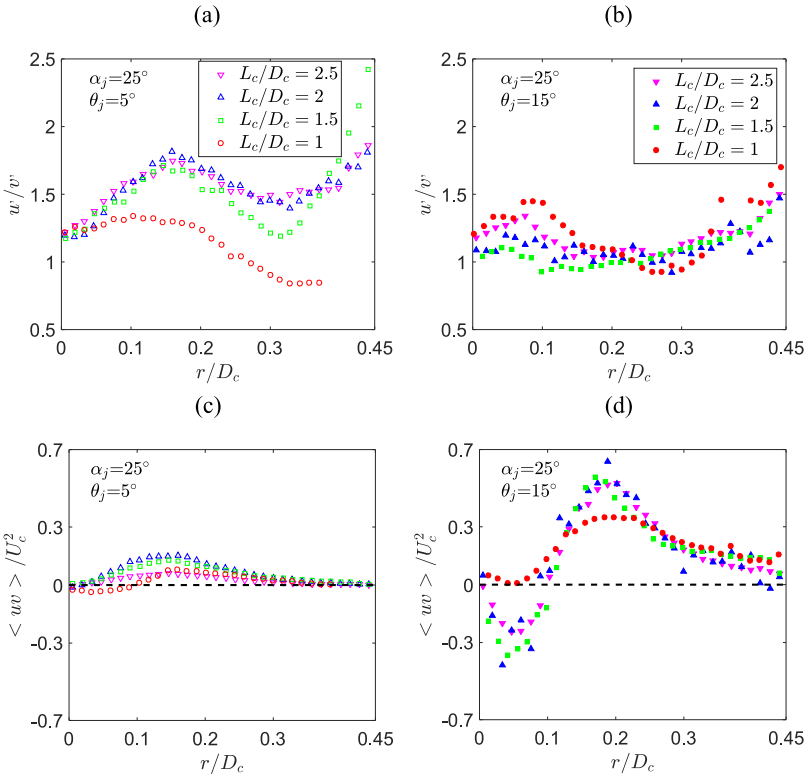

FIG. 8. Radial profiles of the ratio of axial and radial RMS velocities (u'/v') and the Reynolds shear stresses ($\langle uv \rangle / U^2{}_c$) at the merging point for the cases of (a) and (c) α_j = 25° and θ_j = 5°, (b) and (d) α_j = 25° and θ_j = 15°, and for aspect ratios of L_c/D_c = 2.5, 2, 1.5, and 1. Here D_c denotes the diameter of the MIJCC and the legends are identical to all cases with the same θ_j.

the jet and surrounding flow within the jet interaction region. However, the value of $\langle uv \rangle / U^2{}_c$ is typically greater for the higher-swirl cases than that for the low-swirl cases. That is, although the degree of anisotropy at the merging point is greater for $\theta_j = 5°$, the extent of large-scale flow motion at this point is greater for $\theta_j = 15°$ than that for $\theta_j = 5°$, regardless of the value of L_c/D_c. This evidence supports the finding that the interaction between multiple jets is stronger for high-swirl jet configurations.[39]

Figure 9 presents the integral length scale normalized by the nozzle diameter (L_u/D_{pipe}) along the centerline of the MIJCC for all experimental conditions. The integral length

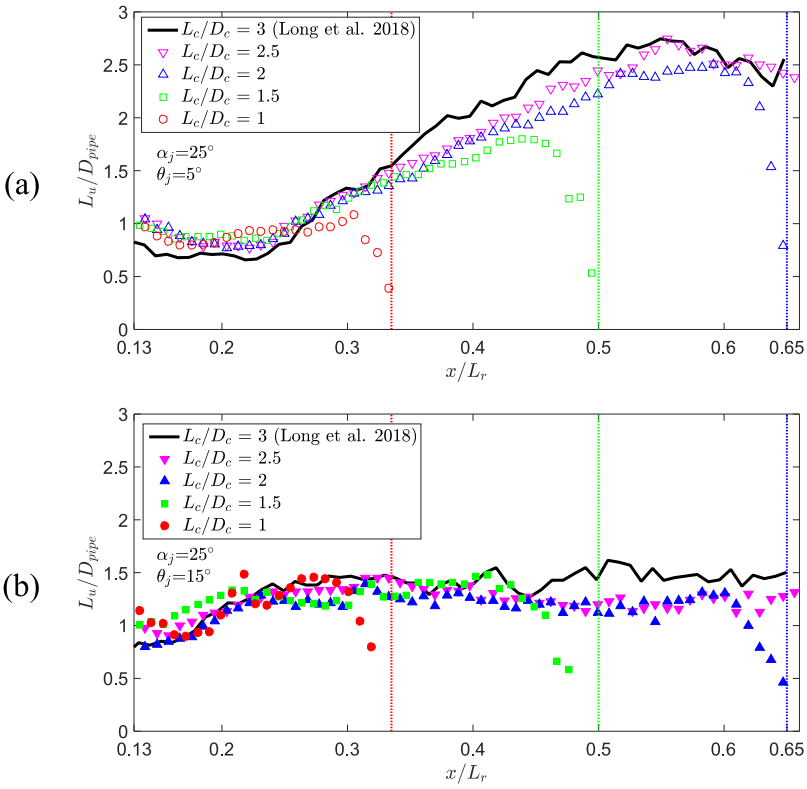

FIG. 9. Evolution of the integral length scale [see Eq. (3)] along the axis of the MIJCC device normalized by the nozzle diameter (D_{pipe}), as a function of the reference chamber length (L_r) for the cases of (a) α_j = 25° and θ_j = 5°, (b) α_j = 25° and θ_j = 15°, and for aspect ratios of L_c/D_c = 1–3. For clarity, only one in two data points is presented.

scale (L_u) is defined as

$$L_u = \int_0^{r_0} \langle u(x)u(x+r)\rangle \left\langle u^2 \right\rangle^{-1} dr, \tag{3}$$

where $u(x)$ denotes the fluctuating component of the axial velocity and r_0 corresponds to the first zero crossing of the cross-correlation function $\langle u(x)u(x+r)\rangle \left\langle u^2 \right\rangle^{-1}$, following Xu and Antonia.[36] The published data for the case of $L_c/D_c = 3$[11] are included for reference. The uncertainty associated with L_u was estimated to be less than 10% from a sensitivity study of the spatial resolution and literature data.[11,40] For the cases of $\theta_j = 5°$ [Fig. 9(a)], where the flow is characterized by a clear resulting central jet flow, it can be seen that, for all L_c/D_c, the value of L_u/D_{pipe} first decreases between $0.13 \le x/L_r \le 0.23$, which corresponds approximately to the region upstream from the merging point, before increasing approximately linearly for $x/L_r > 0.23$. This near linear increase in L_u/D_{pipe} with axial distance is consistent with free-jet measurements.[40] However, as L_c/D_c is decreased from 3 to 1, the slope and magnitude of L_u/D_{pipe} decrease so that a significant drop in L_u/D_{pipe} occurs at the end of the chamber (the bluff end-wall) for all cases. That is, a decrease in L_c/D_c tends to decrease the large-scale flow motion along the centerline of the chamber for $\theta_j = 5°$ configurations, consistent with the findings in Fig. 8. For the configurations of $\theta_j = 15°$ [Fig. 9(b)], the value of L_u/D_{pipe} increases linearly upstream from the stagnation point ($x/L_r \approx 0.3$) and then remains almost the same value along the axis of the chamber for all cases. However, the evolution of L_u/D_{pipe} is almost independent of L_c/D_c, although a drop in L_u/D_{pipe} is also observed at the end of the chamber due to the effect of the bluff end-wall. This finding, together with the evolution of u'/U_e and v'/U_e presented in Fig. 6, provides further evidence that the degree of large-scale flow oscillations tends to increase with L_c/D_c for cases where the swirl component is weak (here $\theta_j = 5°$).

C. Quantification of the recirculation rate

Figure 10 presents the effect of the chamber aspect ratio L_c/D_c on the recirculation rate (K_v) within the MIJCC configurations for all experimental conditions. The recirculation rate K_v is defined as

$$K_v = \dot{m}_{ent}/\dot{m}_{in}, \tag{4}$$

where

$$\dot{m}_{ent} = \int_0^{r} 2\pi r \rho U_{ent} dr \tag{5}$$

is the total mass flow rate of fluid entrained by all inlet jets transported upstream through a plane orthogonal to the axis at the plane x/L_c. Equation (5) was adapted from the calculation of the entrainment rate from the previous study of the jet,[41–43] where the entrainment velocity, U_{ent}, refers to the negative axial velocity ($U_x < 0$) within the chamber, while the positive axial velocity was excluded from the calculation. The symbol of $\dot{m}_{in}$ refers to the total inlet mass flow rate of fluid.

For the $\theta_j = 5°$ configurations [Fig. 10(a)], the results show that a single hump profile, approximately corresponding to the axial extent of the ERZ, occurs for all cases, while the location of peak K_v [$(K_v)_{max.ERZ}$] coincides well with the location of the vortex-core in the ERZ (x_{core} in Fig. 3).

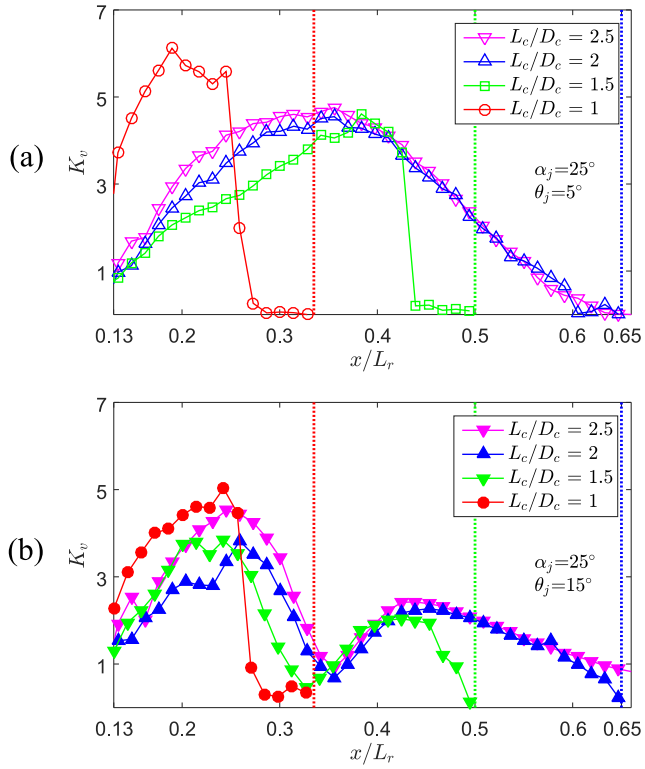

FIG. 10. Evolution of the recirculation rate ($K_v = \dot{m}_{ent}/\dot{m}_{in}$) along the axis of the MIJCC (x/L_r) for the configurations of (a) $\alpha_j = 25°$ and $\theta_j = 5°$, (b) $\alpha_j = 25°$ and $\theta_j = 15°$, and for aspect ratios of $L_c/D_c = 2.5$, 2, 1.5, and 1. For clarity, only one in three data points is presented.

For $L_c/D_c = 2.5$–1.5, a decrease in L_c/D_c tends to decrease the value of K_v throughout the chamber, although $(K_v)_{max.ERZ}$ for all three cases remains approximately the same (occurring at $x/L_r = 0.38$). However, for $L_c/D_c = 1$, $(K_v)_{max.ERZ}$ increases significantly (by 25%) and its location moves further upstream to $x/L_r = 0.2$ due to the confinement effect caused by the chamber length. Hence, the axial profile of K_v is consistent for $L_c/D_c \ge 2$, while as L_c is further reduced to 1, both the value and distribution of K_v are strongly restricted by the reduced chamber length.

For the $\theta_j = 15°$ configurations [Fig. 10(b)], it can be seen that a double-hump profile occurs for all cases in which both ERZ and CRZ are present (see Fig. 3). Furthermore, for each given case of L_c/D_c, the maximum value of K_v in ERZ [$(K_v)_{max.ERZ}$] is approximately 50% higher than that in CRZ [$(K_v)_{max.CRZ}$]. This implies that the circulation strength in ERZ is similarly stronger.[11] In addition, the maximum value of K_v is almost independent of L_c/D_c for both the ERZ and CRZ regions, although the axial extent where $K_v > 0$ is reduced by 50% for a decreased L_c/D_c.

The results in Fig. 10 also show that the value of $(K_v)_{max.ERZ} > 3$ for all cases considered here, regardless of L_c/D_c. This is an important finding for the development of practical combustion applications, particularly those employing combustion in the MILD (moderate or intense low-oxygen dilution) regime because it implies the presence of a large and uniform recirculation zone, which is important for the MILD combustion regime, suggesting strong potential for a quasi-homogeneous temperature.[28,30]

D. Effects of the chamber aspect ratio

Table IV presents a summary of the location of the jet merging point (x_{mer}/L_r), stagnation point (x_s/L_r), and the CRZ axial extent (x_{CRZ}/L_r) along the axis of the MIJCC for all chamber aspect ratios investigated in the present study. Here x_{CRZ} denotes the maximum axial location of the CRZ region. It can be seen from the table that all critical locations change significantly as the L_c/D_c is reduced.

Figure 11 presents the characteristic centerline length of (a) the stagnation point (Δx_s), (b) the CRZ region (Δx_{CRZ}), and (c) the ERZ region (Δx_{ERZ}), normalized by the diameter of the chamber (D_c), as a function of the aspect ratio L_c/D_c. As shown in the inset, we define $\Delta x_s = (L_c - x_s)$ as the distance between the stagnation point and the bluff end-wall, $\Delta x_{ERZ} = (x_s - x_{mer})$ refers to the distance between the merging and stagnation points, and $\Delta x_{CRZ} = (x_{CRZ} - x_s)$ denotes the distance between the stagnation and CRZ points. The data points for $L_c/D_c = 3$, which were measured from our previous study but not previously published, are also included. All measured data points are labelled with solid makers, while some "extrapolated" points, which are labelled with hollow markers, are extrapolated from the values in Table IV.

For Fig. 11(a), it can be seen that Δx_s increases linearly with the aspect ratio L_c/D_c in the range $1 \le L_c/D_c \le 3$ for the high-swirl cases ($\theta_j = 15°$) and $2 \le L_c/D_c \le 3$ for the low-swirl cases ($\theta_j = 5°$). For the latter case, the value of $\Delta x_s \approx 0$ occurs for $L_c/D_c \le 2$, which suggests that $L_{c.crit}/D_c = 2$ is the critical chamber length where the bluff end-wall starts to significantly impact the ERZ and the resulting flow. Conversely, it can also be inferred that for $L_c > L_{c,crit}$, the chamber length does not significantly influence the ERZ within the cylindrical chamber. For the higher-swirl cases ($\theta_j = 15°$), the values of Δx_s are larger than the low-swirl cases due to the decreased axial extent of the ERZ. Hence, the value of $L_{c.crit}$ is approximately equal to D_c for these configurations ($L_{c.crit}/D_c = 1$).

The trends for Δx_{CRZ} in Fig. 11(b) are qualitatively similar to those for Δx_s. That is, a decrease in the aspect ratio L_c/D_c significantly decreases the value of $\Delta x_{CRZ}/D_c$ for both the $\theta_j = 5°$ and $\theta_j = 15°$ configurations. The value of $\Delta x_{CRZ}/D_c$ reduces from 0.45 at $L_c/D_c = 3$ to 0 at $L_c/D_c = 2$ for $\theta_j = 5°$ configurations, while for $\theta_j = 15°$ cases, the value of $\Delta x_{CRZ}/D_c$ decreases from 1.55 at $L_c/D_c = 3$ to 0 at $L_c/D_c = 1$. The value of $\Delta x_{CRZ}/D_c$ is important for quantifying the effect of L_c/D_c on the CRZ region since the critical value of $\Delta x_{CRZ.crit}/D_c = 0$ indicates the absence of the CRZ within the cylindrical chamber. Hence, a decrease in the value of L_c/D_c from 3 to 1 leads to a reduction in the size of the CRZ for both configurations,

TABLE IV. Normalized axial location of the jet merging and stagnation points, and the CRZ axial extent along the centerline of the MIJCC.

Experiment case no.	Configurations	Jet merging point (x_{mer}/L_r)	Stagnation point (x_s/L_r)	CRZ point (x_{CRZ}/L_r)
1	MIJCC-05-LD25	0.27	0.65	>0.65
2	MIJCC-05-LD20	0.27	0.65	N/A
3	MIJCC-05-LD15	0.27	0.50	N/A
4	MIJCC-05-LD10	0.27	0.33	N/A
5	MIJCC-15-LD25	0.21	0.29	>0.65
6	MIJCC-15-LD20	0.21	0.29	0.65
7	MIJCC-15-LD15	0.19	0.27	0.48
8	MIJCC-15-LD10	0.24	0.32	N/A
9*	MIJCC-05-LD30	0.27	0.65	>0.65
10*	MIJCC-15-LD30	0.21	0.28	>0.65

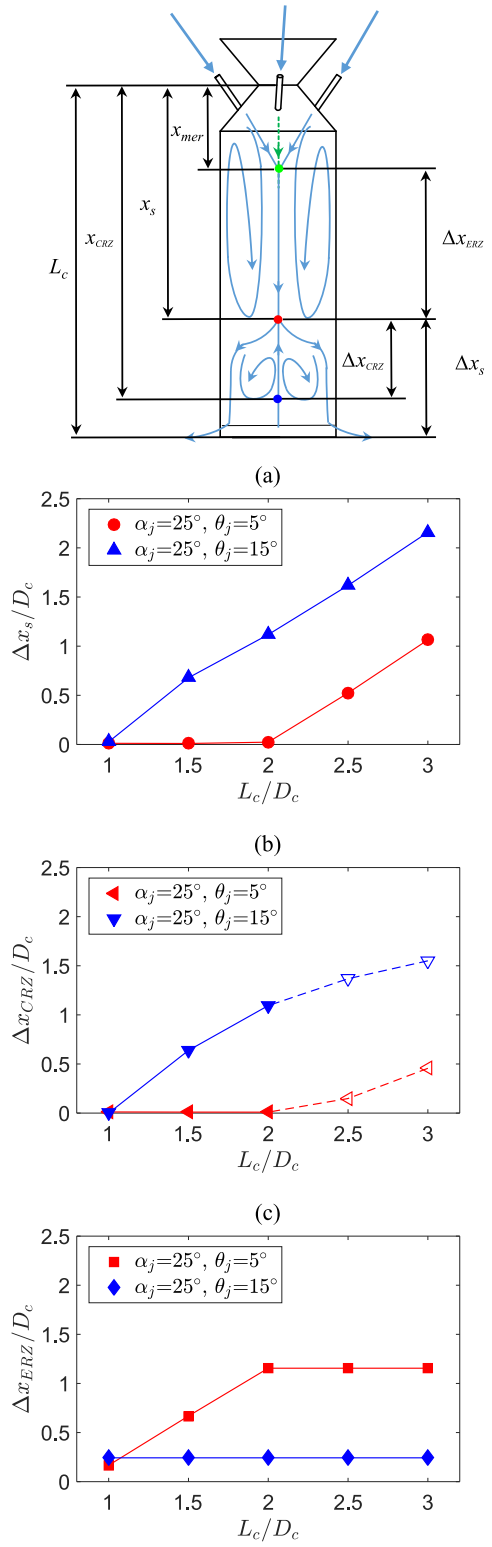

FIG. 11. Characteristic length of (a) the stagnation point (Δx_s), (b) the CRZ region (Δx_{CRZ}), and (c) the ERZ region (Δx_{ERZ}), normalized by the diameter of the chamber (D_c), as a function of the chamber aspect ratio L_c/D_c.

TABLE V. Definition of flow regimes and their key controlling parameters in the MIJCC configurations equipped with multiple jets for $\alpha_j = 25°$ and $\theta_j = 5°, 15°$.

Flow regime		Controlling parameters	Resulting parameters	ERZ	CRZ	Resulting flow
Regime I	Decreasing L_c/D_c	α_j and θ_j	$\Delta x_s/D_c > 0$ $\Delta x_{CRZ}/D_c > 0$ $\Delta x_{ERZ}/D_c > 0$	Yes	Yes	Yes
Regime II		α_j and θ_j L_c/D_c	$\Delta x_s/D_c = 0$ $\Delta x_{CRZ}/D_c = 0$ $\Delta x_{ERZ}/D_c > 0.2$	Yes	No	Yes
Regime III		α_j and θ_j L_c/D_c x_{mer}	$\Delta x_s/D_c = 0$ $\Delta x_{CRZ}/D_c = 0$ $\Delta x_{ERZ}/D_c \leq 0.2$	Yes	No	No

while the absence of the CRZ region occurs for $L_c/D_c \leq 2$ and 1 for $\theta_j = 5°$ and 15° configurations, respectively.

It can also be seen from Fig. 11(c) that for $\theta_j = 5°$ configurations, the value of $\Delta x_{ERZ}/D_c = 1.2$ for all cases where $L_c/D_c \geq 2$. This means that the bluff-end wall only impacts the CRZ and does not influence the ERZ. This, in turn, implies that the CRZ vortex is somewhat decoupled from the ERZ vortex for $L_c/D_c \geq 2$. In addition, the value of $\Delta x_{ERZ}/D_c$ significantly decreases from 1.2 to 0.1 as L_c/D_c is further decreased to 1. By contrast, the value of $\Delta x_{ERZ}/D_c \approx 0.3$ is almost independent of L_c/D_c within the range of $1 \leq L_c/D_c \leq 3$ for $\theta_j = 15°$ configurations. This is because the bluff end-wall only impacts the upstream ERZ for $L_c/D_c \leq 1$ due to the shorter axial extent of the ERZ for $\theta_j = 15°$. The parameter of $\Delta x_{ERZ}/D_c$ quantifies the effect of the aspect ratio L_c/D_c on both the ERZ and the jet merging point, which means that for the cases where $\Delta x_{ERZ}/D_c$ approaches 0, the inlet-jets impinge on the bluff end-wall instead of generating a resulting flow. Hence, the value of L_c/D_c significantly influences the interaction of multiple jets for $L_c/D_c \leq 1$, for all values of θ_j.

It is also worth noting that, for the values of L_c/D_c considered here, a reduction in L_c/D_c leads to a significant decrease in the difference between the values of $\Delta x_s/D_c$, $\Delta x_{ERZ}/D_c$, and $\Delta x_{CRZ}/D_c$ for both the $\theta_j = 5°$ and $\theta_j = 15°$ configurations. For example, the difference in $\Delta x_s/D_c$ between $\theta_j = 5°$ and $\theta_j = 15°$ reduces from $\Delta(\Delta x_s/D_c) = 1.1$ at $L_c/D_c = 3$ to $\Delta(\Delta x_s/D_c) = 0$ at $L_c/D_c = 1$. This, in turn, suggests that as the aspect ratio L_c/D_c is reduced from 3 to 1, the significance of L_c/D_c on the larger-scale recirculation zones within the MIJCC increases, while the significance of θ_j decreases substantially.

E. Identification of the key controlling parameters for flow regimes

Table V summarizes the key parameters for controlling the three distinctive flow regimes that have been identified within the rotationally symmetric MIJCC configurations for a fixed value of $\alpha_j = 25°$ but with $\theta_j = 5°$ and 15°, and a decrease value of the chamber aspect ratio L_c/D_c from 3 to 1, using both the flow visualization and quantitative data. The three flow regimes are shown schematically in Fig. 12, and the detailed description are presented in Secs. III E 1–III E 3.

1. Regime I: External and central recirculation zones

Regime I is characterized by the presence of both external and central recirculation zones [ERZ (red dashed box) and CRZ (purple dotted box)] within the MIJCC. The relative significance of the ERZ and CRZ depends strongly on the value of jet angles (α_j and θ_j), which is consistent with our previous work,[10,11] while the aspect ratio L_c/D_c has a negligible influence on the large-scale flow structure in this regime.

2. Regime II: External recirculation zone with a resulting flow

Regime II is characterized by the presence of a dominant ERZ generated from the resulting flow within the MIJCC. The effect of the aspect ratio L_c/D_c significantly reduces the position and strength of the ERZ due to the increased confinement

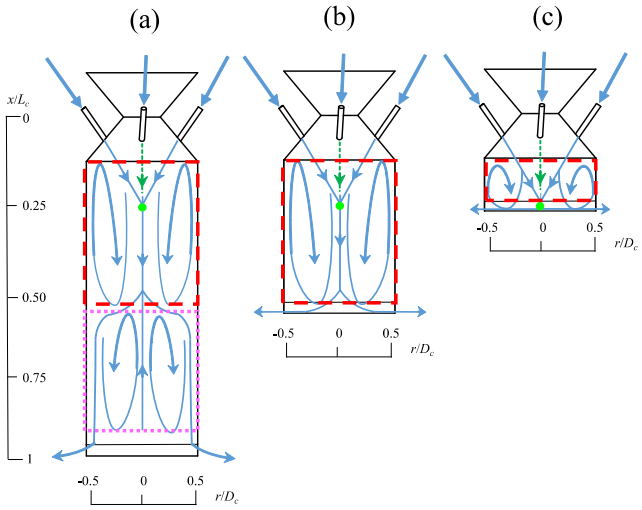

FIG. 12. Schematic diagrams of the three distinctive flow regimes that have been identified within the MIJCC configurations for aspect ratios of L_c/D_c = 1–3. (a) Regime I: External and central recirculation zones. (b) Regime II: External recirculation zone with a resulting flow. (c) Regime III: External recirculation zone with no resulting flow.

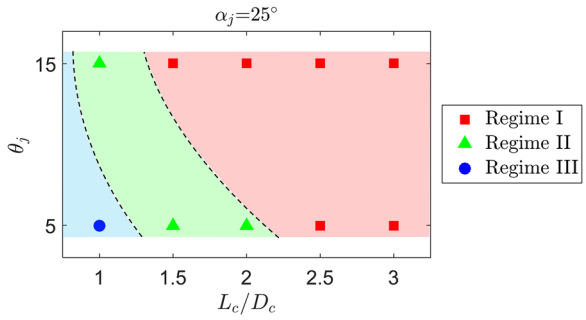

FIG. 13. Map of the three dominant flow regimes that have been identified within the MIJCC configurations for the jet inclination angle α_j = 25° and two jet azimuthal angles θ_j = 5° and 15°, and for chamber aspect ratios L_c/D_c = 1–3.

caused by the bluff end-wall. The influence of jet angles (α_j and θ_j) remains significant in this regime, although it is not as prominent as that in Regime I.

3. Regime III: External recirculation zone with no resulting flow

Regime III is characterized by the presence of dominant ERZ generated from the multiple inlet-jets, which runs the entire chamber of the MIJCC. Owing to the significantly reduced value in L_c/D_c, the inlet-jets have insufficient space to generate a resulting flow downstream from the merging point. Therefore, the size of the ERZ is further reduced and the strength of the ERZ is the strongest.

Figure 13 presents a regime map as a function of the chamber aspect ratio L_c/D_c and jet azimuthal angles (θ_j) for the MIJCC configurations of α_j = 25°. It can be seen that the transition between each regime occurs for $L_c/D_c \approx 2$ and 1 for θ_j = 5° configurations, and $L_c/D_c \approx 1$ and <1 for θ_j = 15° configurations. This implies that a higher value of θ_j reduces the critical value of L_c/D_c. This is because a higher value in θ_j results in less impingement among inlet-jets, a weaker resulting flow, and a higher swirl, which in turn decreases the axial extent of the ERZ and CRZ. Hence, it can be concluded that, for both the low-swirl (θ_j = 5°) and high-swirl (θ_j = 15°) configurations, the flow patterns are strongly controlled by the combination of the jet azimuthal angle (θ_j) and the chamber aspect ratio (L_c/D_c), with the significance of L_c/D_c increases as L_c/D_c decreases.

IV. CONCLUSIONS

New quantitative information has been provided on the iso-thermal flow field within a cylindrical chamber featuring multiple jets with an inclination angle α_j = 25° and two azimuthal angles θ_j = 5° and 15° for a range of chamber aspect ratios (L_c/D_c). Three distinctive flow regimes were identified within the Multiple Impinging Jet in a Cylindrical Chamber (MIJCC) as follows:

a. Regime I ($L_c/D_c > 2$ for θ_j = 5° or $L_c/D_c > 1$ for θ_j = 15°): External and central recirculation zones.
b. Regime II ($L_c/D_c > 1$ for θ_j = 5° or L_c/D_c = 1 for θ_j = 15°): External recirculation zone with a distinctive resulting flow.
c. Regime III ($L_c/D_c \leq 1$ for θ_j = 5° or $L_c/D_c < 1$ for θ_j = 15°): External recirculation zone with no resulting flow.

The key findings of the study are as follows:

1. The presence of each flow regime is strongly controlled by the combination of the jet angles (α_j and θ_j) and the chamber aspect ratio (L_c/D_c), with the significance of L_c/D_c increases as the value of L_c/D_c is decreased from 3 to 1.
2. The flow field within the ERZ immediately downstream from the jet merging point in Regime I is approximately independent of the length of the cavity L_c. However, in Regimes II and III, the characteristics of the ERZ depend strongly on L_c.
3. For $\theta_j > 0°$ cases, the decay of the central resulting flow downstream from the jet merging point is significantly greater than for θ_j = 0° (single jet or multiple jets). The value of mean axial velocity (U_c) along the axis of the chamber was found to increase by approximately 40% from Regime I to Regime II, while it decreases significantly (by 50%) for Regime III. This indicates that the effect of the aspect ratio L_c/D_c depends strongly on the presence or absence of the resulting flow downstream from the merging point.
4. The significance of the large-scale oscillations (e.g., jet precession) and the velocity fluctuations (u' and v') was found to increase with the chamber aspect ratio L_c/D_c for those configurations where the ERZ is dominant (θ_j = 5°). However, the influence of L_c/D_c on flow unsteadiness was found to be relatively small for those configurations generating a dominant CRZ (θ_j = 15°). This is evidenced by a higher value of Reynolds shear stress ($\langle uv \rangle / U^2_c$) for all L_c/D_c cases at the merging point for θ_j = 15° than for θ_j = 5°.
5. The large-scale flow motion corresponding to the integral length scale (L_u) was found to be inhibited as L_c/D_c is decreased for the case where a swirl is relatively weak (θ_j = 5°), while it is almost independent from L_c/D_c for higher-swirl cases (θ_j = 15°). This indicates a reduced influence of the chamber aspect ratio on the turbulent velocity field for θ_j = 15° cases.
6. The value of the recirculation rate (K_v) was found to increase by 25% as L_c/D_c is reduced from 3 to 1 (Regime I to Regime III), although the axial extent of K_v reduces by 50%. The value of K_v exceeds 3 for all cases, which has been found by others to be an important indicator for the avoidance of combustion reactants impinging on the walls and also maintaining a relatively high recirculation rate ($K_v \geq 3$).

ACKNOWLEDGMENTS

We acknowledge the support of the Australian Research Council, FCT Combustion Pty. Ltd., and Vast Solar Pty. Ltd. through the ARC Linkage Grant No. LP110200060. Mr. Shen Long acknowledges the financial support of the Australian Government Research Training Program. Finally, we gratefully acknowledge the anonymous reviewers who provided constructive feedback to strengthen the paper.

[1]E. Koepf, W. Villasmil, and A. Meier, "High temperature flow visualization and aerodynamic window protection of a 100-kWth solar thermochemical receiver-reactor for ZnO dissociation," Energy Procedia **69**, 1780 (2015).

[2]G. Cox, "Multiple jet correlations for gas turbine engine combustor design," J. Eng. Power **98**, 265 (1976).

[3]T. Chammem, H. Mhiri, and O. Vauquelin, "Experimental and computational investigation of Reynolds number effect on the longitudinal ventilation in large enclosure of twin inclined jets," Build. Environ. **67**, 87 (2013).

[4]T. Boushaki and J.-C. Sautet, "Characteristics of flow from an oxy-fuel burner with separated jets: Influence of jet injection angle," Exp. Fluids **48**, 1095 (2010).

[5]H. Becker and B. Booth, "Mixing in the interaction zone of two free jets," AIChE J. **21**, 949 (1975).

[6]J. A. Fitzgerald and S. V. Garimella, "A study of the flow field of a confined and submerged impinging jet," Int. J. Heat Mass Transfer **41**, 1025 (1998).

[7]R. C. Deo, J. Mi, and G. J. Nathan, "The influence of Reynolds number on a plane jet," Phys. Fluids **20**, 075108 (2008).

[8]G. J. Nathan, D. Battye, and P. Ashman, "Economic evaluation of a novel fuel-saver hybrid combining a solar receiver with a combustor for a solar power tower," Appl. Energy **113**, 1235 (2014).

[9]J. H. Lim, A. Chinnici, B. B. Dally, and G. J. Nathan, "Assessment of the potential benefits and constraints of a hybrid solar receiver and combustor operated in the MILD combustion regime," Energy **116**(Part 1), 735 (2016).

[10]S. Long, T. C. W. Lau, A. Chinnici, Z. F. Tian, B. B. Dally, and G. J. Nathan, "Experimental and numerical investigation of the iso-thermal flow characteristics within a cylindrical chamber with multiple planar-symmetric impinging jets," Phys. Fluids **29**, 105111 (2017).

[11]S. Long, T. C. W. Lau, A. Chinnici, Z. F. Tian, B. B. Dally, and G. J. Nathan, "Iso-thermal flow characteristics of rotationally symmetric jets generating a swirl within a cylindrical chamber," Phys. Fluids **30**, 055110 (2018).

[12]J. H. Lim, G. J. Nathan, E. Hu, and B. B. Dally, "Analytical assessment of a novel hybrid solar tubular receiver and combustor," Appl. Energy **162**, 298 (2016).

[13]E. Tanaka, "The interference of two-dimensional parallel jets: 1st report, experiments on dual jet," Bull. JSME **13**, 272 (1970).

[14]E. Tanaka, "The interference of two-dimensional parallel jets: 2nd report, experiments on the combined flow of dual jet," Bull. JSME **17**, 920 (1974).

[15]E. Tanaka and S. Nakata, "The interference of two-dimensional parallel jets: 3rd report, the region near the nozzles in triple jets," Bull. JSME **18**, 1134 (1975).

[16]Z. Gao, J. Han, Y. Xu, Y. Bao, and Z. Li, "Particle image velocimetry (PIV) investigation of flow characteristics in confined impinging jet reactors," Ind. Eng. Chem. Res. **52**, 11779 (2013).

[17]T. Guo, M. J. Rau, P. P. Vlachos, and S. V. Garimella, "Axisymmetric wall jet development in confined jet impingement," Phys. Fluids **29**, 025102 (2017).

[18]S. Beltaos and N. Rajaratnam, "Impingement of axisymmetric developing jets," J. Hydraul. Res. **15**, 311 (1977).

[19]G. M. Carlomagno and A. Ianiro, "Thermo-fluid-dynamics of submerged jets impinging at short nozzle-to-plate distance: A review," Exp. Therm. Fluid Sci. **58**, 15 (2014).

[20]Y. Varol and H. F. Oztop, "Buoyancy induced heat transfer and fluid flow inside a tilted wavy solar collector," Build. Environ. **42**, 2062 (2007).

[21]D. Rockwell and E. Naudascher, "Self-sustaining oscillations of flow past cavities," J. Fluids Eng. **100**, 152 (1978).

[22]V. Prasad and F. A. Kulacki, "Convective heat transfer in a rectangular porous cavity—Effect of aspect ratio on flow structure and heat transfer," J. Heat Transfer **106**, 158 (1984).

[23]G. K. Morris and S. V. Garimella, "Orifice and impingement flow fields in confined jet impingement," J. Electron. Packag. **120**, 68 (1998).

[24]G. Morris, S. Garimella, and J. Fitzgerald, "Flow-field prediction in submerged and confined jet impingement using the Reynolds stress model," J. Electron. Packag. **121**, 255 (1999).

[25]S. V. Garimella and R. Rice, "Confined and submerged liquid jet impingement heat transfer," J. Heat Transfer **117**, 871 (1995).

[26]S. A. Al-Sanea, M. F. Zedan, and M. B. Al-Harbi, "Effect of supply Reynolds number and room aspect ratio on flow and ceiling heat-transfer coefficient for mixing ventilation," Int. J. Therm. Sci. **54**, 176 (2012).

[27]Y.-H. Kao, S. B. Tambe, and S.-M. Jeng, "Effect of chamber length with converging exhaust on swirling flow field characteristics of a counter-rotating radial-radial swirler," in *ASME Turbo Expo 2013: Turbine Technical Conference and Exposition* (American Society of Mechanical Engineers, 2013), p. V01BT04A026.

[28]J. Wünning and J. Wünning, "Flameless oxidation to reduce thermal NO-formation," Prog. Energy Combust. Sci. **23**, 81 (1997).

[29]J. Mi, F. Wang, P. Li, and B. Dally, "Modified vitiation in a moderate or intense low-oxygen dilution (MILD) combustion furnace," Energy Fuels **26**, 265 (2011).

[30]G. Szegö, B. Dally, and G. Nathan, "Operational characteristics of a parallel jet MILD combustion burner system," Combust. Flame **156**, 429 (2009).

[31]J. Nikuradse, "Gesetzmäßigkeiten der turbulenten Strömung in glatten Rohren," Forsch. Geb. Ingenieurwes. **4**, 44 (1933).

[32]N. Grosjean, L. Graftieaux, M. Michard, W. Hübner, C. Tropea, and J. Volkert, "Combining LDA and PIV for turbulence measurements in unsteady swirling flows," Meas. Sci. Technol. **8**, 1523 (1997).

[33]N. Syred, "A review of oscillation mechanisms and the role of the precessing vortex core (PVC) in swirl combustion systems," Prog. Energy Combust. Sci. **32**, 93 (2006).

[34]Y. Liu, M. G. Olsen, and R. O. Fox, "Turbulence in a microscale planar confined impinging-jets reactor," Lab Chip **9**, 1110 (2009).

[35]L. Chua and A. Lua, "Measurements of a confined jet," Phys. Fluids **10**, 3137 (1998).

[36]G. Xu and R. Antonia, "Effect of different initial conditions on a turbulent round free jet," Exp. Fluids **33**, 677 (2002).

[37]G. J. Nathan, J. Mi, Z. T. Alwahabi, G. J. R. Newbold, and D. S. Nobes, "Impacts of a jet's exit flow pattern on mixing and combustion performance," Prog. Energy Combust. Sci. **32**, 496 (2006).

[38]T. C. Lau and G. J. Nathan, "The effect of Stokes number on particle velocity and concentration distributions in a well-characterised, turbulent, co-flowing two-phase jet," J. Fluid Mech. **809**, 72 (2016).

[39]M. Vanierschot and E. Van den Bulck, "Influence of swirl on the initial merging zone of a turbulent annular jet," Phys. Fluids **20**, 105104 (2008).

[40]J. Mi and G. J. Nathan, "Statistical properties of turbulent free jets issuing from nine differently-shaped nozzles," Flow, Turbul. Combust. **84**, 583 (2010).

[41]S. Park and H. Shin, "Measurements of entrainment characteristics of swirling jets," Int. J. Heat Mass Transfer **36**, 4009 (1993).

[42]J. Panda and D. McLaughlin, "Experiments on the instabilities of a swirling jet," Phys. Fluids **6**, 263 (1994).

[43]M. Amielh, T. Djeridane, F. Anselmet, and L. Fulachier, "Velocity near-field of variable density turbulent jets," Int. J. Heat Mass Transfer **39**, 2149 (1996).